Kynurenine–3–monooxygenase inhibition prevents multiple organ failure in rodent models of acute pancreatitis

Kynurenine–3–monooxygenase inhibition prevents multiple organ failure in rodent models of acute pancreatitis.

Damian J Mole[1,2], Scott P Webster[3], Iain Uings[4], Xiaozhong Zheng[1], Margaret Binnie[3], Kris Wilson[3], Jonathan P Hutchinson[5], Olivier Mirguet[6], Ann Walker[4], Benjamin Beaufils[6], Nicolas Ancellin[6], Lionel Trottet[6], Véronique Bénéton[6], Christopher G Mowat[7], Martin Wilkinson[7], Paul Rowland[5], Carl Haslam[5], Andrew McBride[3], Natalie ZM Homer[8], James E Baily[3], Matthew GF Sharp[9], O James Garden[2], Jeremy Hughes[1], Sarah EM Howie[1], Duncan S Holmes[4], John Liddle[4] and John P Iredale[1].

Affiliations

1. Medical Research Council Centre for Inflammation Research, University of Edinburgh, UK
2. Clinical Surgery, University of Edinburgh, UK
3. University/British Heart Foundation Centre for Cardiovascular Science, University of Edinburgh, UK
4. Discovery Partnerships with Academia, GlaxoSmithKline, Stevenage, UK
5. Molecular Discovery Research, GlaxoSmithKline, Stevenage, UK
6. Flexible Discovery Unit, GlaxoSmithKline, Paris, France.
7. EastChem School of Chemistry, University of Edinburgh, UK
8. Mass Spectrometry Core, University of Edinburgh, UK
9. Central Bioresearch Services, University of Edinburgh, UK

Corresponding author

Damian J. Mole

Email: damian.mole@ed.ac.uk

Abstract

Acute pancreatitis (AP) is a common and devastating inflammatory condition of the pancreas that is considered to be a paradigm of sterile inflammation leading to systemic multiple organ dysfunction syndrome (MODS) and death[1,2] Acute mortality from AP-MODS exceeds 20%[3] and for those who survive the initial episode, their lifespan is typically shorter than the general population[4]. There are no specific therapies available that protect individuals against AP-MODS. Here, we show that kynurenine-3-monooxygenase (KMO), a key enzyme of tryptophan metabolism[5], is central to the pathogenesis of AP-MODS. We created a mouse strain deficient for *Kmo* with a robust biochemical phenotype that protected against extrapancreatic tissue injury to lung, kidney and liver in experimental AP-MODS. A medicinal chemistry strategy based on modifications of the kynurenine substrate led to the discovery of GSK180 as a potent and specific inhibitor of KMO. The binding mode of the inhibitor in the active site was confirmed by X-ray co-crystallography at 3.2 Å resolution. Treatment with GSK180 resulted in rapid changes in levels of kynurenine pathway metabolites *in vivo* and afforded therapeutic protection against AP-MODS in a rat model of AP. Our findings establish KMO inhibition as a novel therapeutic strategy in the treatment of AP-MODS and open up a new area for drug discovery in critical illness.

Systemic tryptophan metabolism in mammals occurs primarily via the kynurenine pathway (**Fig. 1a**)[5]. Tryptophan metabolites contribute to acute lung injury in rats with AP[6], while the tryptophan metabolite kynurenine is elevated in blood in humans with severe AP[6]. Sitting at a critical fork in the pathway, kynurenine–3–monooxygenase (KMO) metabolizes kynurenine to 3–hydroxykynurenine, which increases oxidative stress[9], induces apoptosis[10] and is injurious to several cell types[7]. Inhibition of KMO should reduce 3–hydroxykynurenine production which may therefore provide an efficacious strategy to prevent or reduce the severity of extrapancreatic organ injury in AP.

To explore the role of KMO in disease processes we created a mouse strain that lacks KMO activity constitutively in all tissues (**Supplementary Fig. 1a**). Anatomical mapping of tissue *Kmo* mRNA expression in wild-type C57BL6 mice showed high levels of *Kmo* expression in liver and kidney and moderate

Kmo mRNA expression in organs containing secondary lymphoid tissue, specifically lung, spleen, mesenteric lymph node, thymus and peripheral lymph nodes (**Supplementary Fig. 1b**). Mice homozygous for the *Kmo* knockout-first *tm1a* allele (from hereon referred to as Kmo^{null} mice) were shown to have no detectable messenger RNA for *Kmo* in any tissues. Liver homogenates from Kmo^{null} mice lacked the ability to convert kynurenine to 3–hydroxykynurenine, but this activity was restored to wild type levels in mice where the inserted stop signal had been removed ($Kmo^{FRT\text{-}deleted}$ mice) showing that the defect resulted from the specific engineered mutation (**Supplementary Fig. 1c**).

We explored the pathways of kynurenine metabolism by measuring upstream, downstream and alternative pathway metabolites (**Fig. 1b**–**g**). Compared to $Kmo^{FRT\text{-}deleted}$ mice, Kmo^{null} mice show equivalent steady state tryptophan concentrations and profound depletion of 3–hydroxykynurenine ($[\text{tryptophan}]_{\text{plasma}}$ in $Kmo^{FRT\text{-}deleted}$ vs. Kmo^{null} mice: 28 ± 1 μM vs. 28 ± 1 μM, P = 0.843 (t-test); $[\text{3–hydroxykynurenine}]_{\text{plasma}}$ in $Kmo^{FRT\text{-}deleted}$ vs. Kmo^{null} mice: 32 ± 3 nM vs BLQ, P < 0.001 (t-test); n = 5 per group). Kmo^{null} mice have a 19-fold backlog of kynurenine upstream, indicating that KMO is normally the predominant pathway for metabolism of kynurenine ($[\text{kynurenine}]_{\text{plasma}}$ in $Kmo^{FRT\text{-}deleted}$ vs. Kmo^{null} mice: 0.6 ± 0.1 μM vs. 11.0 ± 1.0 μM, P < 0.001 (t-test), n = 5 per group). There is preferential diversion of kynurenine metabolism to kynurenic acid in the Kmo^{null} mice, with steady-state levels 81-fold higher than in $Kmo^{FRT\text{-}deleted}$ mice ($[\text{kynurenic acid}]_{\text{plasma}}$ in $Kmo^{FRT\text{-}deleted}$ vs. Kmo^{null} mice: 0.1 ± 0.0 μM vs. 11.0 ± 1.2 μM; P < 0.001 (t-test), n = 5 per group). Metabolism of kynurenine can also bypass KMO and be converted by kynureninase to anthranilic acid and subsequently to 3–hydroxyanthranilic acid by non-specific hydroxylase activity[5], but this pathway was less active with levels of anthranilic acid only 4-fold higher in Kmo^{null} mice ($[\text{anthranilic acid}]_{\text{plasma}}$ in $Kmo^{FRT\text{-}deleted}$ vs. Kmo^{null} mice: 0.3 ± 0.1 μM vs. 1.0 ± 0.1 μM; P < 0.001 (t-test), n = 5 per group). Kmo^{null} mice have reduced serum 3–hydroxyanthranilic acid concentrations in the steady state, although the reduction is less than observed for 3–hydroxykynurenine ($[\text{3–hydroxyanthranilic acid}]_{\text{plasma}}$ in $Kmo^{FRT\text{-}deleted}$ vs. Kmo^{null} mice: 2.0 ± 0.3 μM vs. 1.1 ± 0.2 μM; P=0.034 (t-test), n = 5 per group). These data support the notion that under normal conditions 3–hydroxyanthranilic acid is

produced primarily via 3–hydroxykynurenine rather than via anthranilic acid, but suggests that the pathway to bypass KMO can function to some degree when KMO is absent. Together, these data show that KMO is the key gatekeeper enzyme that determines the metabolic fate of kynurenine.

We next tested whether the absence of KMO activity affected extrapancreatic organ injury in experimental AP induced by injection of taurocholate into the biliopancreatic duct at laparotomy. Pancreata from sham-operated mice showed normal architecture and no signs of inflammation while those from AP mice showed evidence of necrosis, interlobular edema and a pronounced inflammatory cell infiltrate (**Supplementary Fig 2a**,**b**). No difference in pancreatic injury was noted in Kmo^{null} compared to Kmo^{wt} control mice (**Fig. 2a**) (composite histological score Kmo^{wt} sham vs. AP: 0.0 ± 0.0 vs. 7.1 ± 0.4; Kmo^{null} sham vs. AP: 0.0 ± 0.0 vs. 7.3 ± 0.7; $P < 0.001$ one-way ANOVA across all groups, post hoc Student–Neumann–Keuls (S–N–K) threshold $P < 0.05$ significant for sham vs. AP in both mouse strains, Kmo^{null} AP vs. Kmo^{wt} AP not significant (n.s.); $n =$ 6 or 7 per group). The majority of infiltrating inflammatory cells were positive for the neutrophil marker myeloperoxidase (MPO) by immunohistochemistry (**Supplementary Fig. 2b**) and there was no significant difference in the number of infiltrating neutrophils in the pancreas between Kmo^{null} compared to Kmo^{wt} mice with AP (**Supplementary Fig. 2c**). There was no significant infiltrate of cells positive for the mouse monocyte marker F4/80 (**Supplementary Fig. 2d**). Serum amylase concentration was substantially elevated in AP in both strains but less so in Kmo^{null} compared to Kmo^{wt} mice (**Supplementary Fig. 2e**).

IL-6 trans-signalling has been reported to contribute to extrapancreatic organ injury in experimental mouse AP[8] and indeed serum IL-6 concentrations were elevated in AP compared to sham mice in both Kmo^{wt} and Kmo^{null} mice (**Supplementary Fig. 3a**). There was no statistically significant rise in serum IL-10 in AP in either Kmo^{wt} or Kmo^{null} mice (**Supplementary Fig. 3b**). Kynurenine pathway metabolite levels confirmed the biochemical phenotype seen in unstressed mice and showed a small depletion of tryptophan as a result of AP (**Supplementary Fig. 3c–f**).

The lung is the extrapancreatic organ system most commonly affected in humans with AP. Experimental AP in *Kmo*^{wt} mice generated histological changes consistent with moderate acute respiratory distress syndrome, specifically thickening of the alveolar walls characterized by congestion of alveolar capillaries, interstitial edema and leukocyte infiltrates and exudation of proteinaceous edema fluid into alveolar spaces. This pathology was still detectable in *Kmo*^{null} mice with AP to some degree, although it was much less marked (**Fig. 2b**,**c** and **Supplementary Fig. 4a–d**). MPO-positive infiltrating neutrophils in lung were more numerous during AP in *Kmo*^{wt} compared to *Kmo*^{null} mice (**Supplementary Fig. 4e**). Experimental AP increased the number of apoptotic cells in both strains, significantly so in *Kmo*^{wt} mice (**Fig. 2d**) (*Kmo*^{wt} sham vs. AP: 3 ± 1 vs. 21 ± 9 TUNEL-positive cells/10^6 pixels; *Kmo*^{null} sham vs. AP: 2 ± 0 vs. 6 ± 1 TUNEL-positive cells/10^6 pixels; $P = 0.033$ one-way ANOVA across all groups, post hoc S-N-K threshold $P < 0.05$ significant for *Kmo*^{wt} sham vs. AP and *Kmo*^{wt} AP vs. *Kmo*^{null} AP; *Kmo*^{null} sham vs. AP n.s.; $n = 6$ or 7 per group).

Acute kidney injury (AKI) frequently follows lung injury during AP-MODS in a cumulative manner[9]. Experimental AP led to a dramatic increase in kidney cell apoptosis which was markedly lower in *Kmo*^{null} mice vs. *Kmo*^{wt} controls (**Fig. 2e**) (*Kmo*^{wt} sham vs. AP: 2 ± 0 vs. 18 ± 5 TUNEL-positive cells/10^6 pixels; *Kmo*^{null} sham vs. AP: 1 ± 0 vs. 6 ± 2 TUNEL-positive cells/10^6 pixels; P=0.001 one-way ANOVA across all groups, post hoc S-N-K threshold $P < 0.05$ significant for *Kmo*^{wt} sham vs. AP and *Kmo*^{wt} AP vs. *Kmo*^{null} AP; *Kmo*^{null} sham vs. AP n.s.; $n = 6$ or 7 per group). There was no evidence of histological damage (**Supplementary Fig. 5a–d**) or inflammatory infiltrate (**Supplementary Fig. 5e**,**f**), and no significant functional impairment as creatinine levels were not changed (**Fig. 2f**) ([creatinine]$_{serum}$ *Kmo*^{wt} sham vs. AP: 16 ± 5 vs. 23 ± 5 mmol/L; *Kmo*^{null} sham vs. AP: 5 ± 1 vs. 9 ± 2 mmol/L; $P = 0.019$ one-way ANOVA across all groups, post hoc S-N-K threshold $P < 0.05$ not significant for *Kmo*^{wt} sham vs. AP, *Kmo*^{wt} AP vs. *Kmo*^{null} AP or *Kmo*^{null} sham vs. AP; $n = 5$ to 7 per group). The baseline serum creatinine in *Kmo*^{null} mice appeared lower than in *Kmo*^{wt} mice, although this was not statistically significant.

Experimental AP induced a biochemical liver injury in *Kmo*^{wt} and *Kmo*^{null} mice, but when KMO activity was absent, the magnitude of the rise in alanine

aminotransferase (ALT), a marker of hepatocyte necrosis, was significantly reduced (**Fig. 2g**) ($[ALT]_{plasma}$ *Kmo*^{wt} sham vs. AP: 49 ± 14 vs. 672 ± 68 mmol/L; *Kmo*^{null} sham vs. AP: 38 ± 4 vs. 352 ± 36 mmol/L; $P < 0.001$ one-way ANOVA across all groups, post hoc S-N-K threshold $P < 0.05$ significant for sham vs. AP in both strains and *Kmo*^{wt} AP vs. *Kmo*^{null} AP; $n = 5$ to 7 per group) .

In critically ill individuals, the intravenous route of drug administration is preferred as it provides both ease of administration and control. Several small molecule KMO inhibitors have been reported in the literature for the potential treatment of Huntington's disease[10] but all lack the physicochemical properties required for the clinical development of an intravenous drug. Previous studies suggested that both the carboxylic acid and the carbonyl group present in kynurenine were required for activity[11]. Therefore, a series of propanoic acid heterocycles were prepared which contained H-bond accepting groups to mimic the role of the carbonyl functionality, leading to the discovery of the oxazolidinone GSK180 (**Fig. 3a**).

GSK180 has a half maximum inhibitory concentration (IC_{50}) of approximately 6 nM (mean ± SD pIC_{50} 8.2 ± 0.17 (n = 103)) in a human KMO biochemical assay using human KMO expressed as a GST-fusion protein in a baculovirus expression system[12] (**Fig. 3b**). The observed potency of GSK180 decreased as the concentration of kynurenine was increased showing that the inhibition by GSK180 is competitive with the kynurenine substrate (**Supplementary Fig. 6a**). GSK180 showed negligible activity against other enzymes on the tryptophan pathway (**Supplementary Table 1**), against a panel of over 50 unrelated proteins (**Supplementary Table 2**) and against an additional series of acidergic proteins (**Supplementary Table 3**).

Human KMO was cloned and stably expressed in HEK293 cells where it conferred the ability to convert kynurenine to 3–hydroxykynurenine with an apparent K_m for kynurenine of 78 ± 12 μM (**Supplementary Fig. 6b**). GSK180 has a mean half maximum inhibitory concentration (IC_{50}) of 2.0μM in this cell-based assay (mean pIC_{50} 5.7 ± 0.15 (n = 4)) (**Fig. 3b**). Primary human hepatocytes express endogenous KMO activity, and GSK180 inhibited this activity with comparable potency (IC_{50} = 2.6 μM) (**Fig. 3b**). As the 2-amino-2-(hydroxymethylpropane-1,3-diol) salt (Tris salt), GSK180 has high aqueous

solubility of 24 mg/mL in saline and high microsomal metabolic stability across species (clearance <0.5 ml/min/g in rat, dog, human tissue) (data not shown). Following bolus intravenous injection into rats, GSK180 showed a low volume of distribution and low clearance (Vd_{ss} 0.14 L/kg, $t_{1/2}$ 3 h, Clp 0.45 ml/min/kg at 27 mg/kg i.v. dose) (**Fig. 3c**). GSK180 is thus a low molecular weight (MW 276), highly selective KMO inhibitor with properties suitable for i.v. administration.

The structure of human KMO remains elusive, but that of the yeast orthologue has recently been reported[13]. We utilized KMO from *P. fluorescens* where all the residues surrounding the catalytic site are conserved compared to human KMO, with the exception of His320, which is a phenylalanine in the human protein. Despite this level of conservation, GSK180 demonstrated significantly lower potency against *P. fluorescens* compared to the human construct. (IC_{50} = 500 nM vs. 6 nM, respectively). Nonetheless a 3.2 Å resolution co-crystal structure of GSK180 bound to *P. fluorescens* KMO was solved and revealed significant interactions within the catalytic site (**Fig. 3d)**. The carboxylate forms a salt bridge with Arg84 and forms hydrogen bonds with the side chains of Tyr98 and Asn369. The oxazolidinone carbonyl forms a hydrogen bond with the side chain of the C-terminal domain residue Tyr404 and the 5-chlorine atom forms a π-interaction with Phe238.

Rat *Kmo* was expressed in HEK cells in a manner exactly analogous to the human enzyme described above where the activity showed an apparent K_m for kynurenine of 258 ± 121 μM (**Supplementary Fig. 6c**). GSK180 inhibited rat KMO slightly less potently than the human enzyme, giving an IC_{50} of 7 μM (mean pIC_{50} 5.2 ± 0.09 (*n* = 5)) (**Fig. 3b**). When dosed to rats as an i.v. bolus at 27 mg/kg, the initial concentration of GSK180 was nearly 600 μM in blood (**Fig. 3c**). GSK180 is excluded from rat erythrocytes (blood:plasma ratio of 0.46) and is moderately bound to rat plasma proteins (free fraction 7.7% at 1 mM, *n* = 2)**,** meaning that the peak free drug levels in plasma (92 μM) are >12 fold above the IC_{50} in cells. Indeed, treatment with GSK180 resulted in a rapid increase in circulating levels of both kynurenine and kynurenic acid that returned to baseline as the drug levels dropped (**Fig. 3c**). Levels of 3–hydroxykynurenine in this experiment were too low to be accurately measured. The changes observed in kynurenine are exactly as expected, but the change in kynurenic acid is

curious as the peak occurs prior to the peak of kynurenine suggesting that the increase seen is not simply a result of the increase in availability of substrate.

To explore whether the changes in metabolites observed in the presence of drug were due to inhibition of KMO alone or mediated by another mechanism, GSK180 was dosed to *Kmo*^{wt} and *Kmo*^{null} mice as a single bolus injection at 30 mg/kg which delivered plasma drug levels one hour post dose of 263 ± 98 μM and 351 ± 87 μM respectively. Administration of GSK180 resulted in an increase in kynurenine in the *Kmo*^{wt} mice, but no change was seen in the *Kmo*^{null} mice confirming that this increase results from inhibition of KMO (**Supplementary Fig. 6d**). Curiously GSK180 caused a significant reduction in circulating tryptophan levels in both *Kmo*^{wt} and *Kmo*^{null} mice, suggesting that the compound was having an additional effect unrelated to KMO inhibition. Moreover a clear increase in kynurenic acid was also observed in the *Kmo*^{null} mice, suggesting that the changes observed in kynurenic acid in the presence of compound result both from metabolic diversion as a result of KMO inhibition and an effect on kynurenic acid metabolism that is not mediated by KMO (**Supplementary Fig. 6d**).

On further investigation we confirmed that a similar drop in circulating tryptophan was seen in rats, and moreover that it occurred immediately after compound administration and was stable for several hours, recovering slowly as the plasma level of the compound dropped below 300 μM (**Supplementary Fig. 6e**). Tryptophan is the only amino acid that is bound to plasma proteins and high concentrations of drugs such as salicylate have been shown to compete with this binding[14]. Indeed, GSK180 showed a concentration dependent displacement of tryptophan from plasma proteins in the range equivalent to the exposures observed in this study (**Supplementary Table 4**). However the free tryptophan level remains constant (40 μM (22% of 180 μM) in control and 42 μM (60% of 70 μM) directly after compound administration) suggesting that the displaced tryptophan is distributing rapidly into tissues.

Despite the confounding effects of GSK180 on the pathway outside of KMO inhibition, the dynamics of the change in kynurenine seen following inhibition demonstrate that even under resting conditions flux through KMO is

rapid and is thus consistent with a role for tryptophan metabolism via KMO being an important and early contributory mechanism in AP-MODS.

We next tested the efficacy of GSK180 in protecting against AP-MODS in a well-validated rat model of AP that generates secondary organ dysfunction within 6 hours of the initial insult[6]. GSK180 was given in a therapeutic setting 1 hour after the induction of AP as an i.v. bolus of 24 mg/kg followed by an i.v. infusion of 5.5 mg/kg/hour. This delivered stable plasma drug levels of approximately 600 μM throughout the experiment which resulted in biochemical changes consistent with those seen in the *Kmo*^{null} mouse and in unchallenged animals, namely increased plasma kynurenine and kynurenic acid and decreased plasma tryptophan and 3–hydroxykynurenine (**Supplementary Fig. 7a**).

The experimental model induced pancreatic acinar cell necrosis, edema and an inflammatory cell infiltrate (**Supplementary Fig. 7b**–**d**), with elevated serum amylase at 6 hours (**Supplementary Fig. 7e**). The severity of the histological injury and the magnitude of the serum amylase rise were equivalent in both AP and GSK180-treated groups (**Fig. 4a** and **Supplementary Fig. 7e**). The intense inflammatory cell infiltrate in AP consisted of MPO-positive neutrophils and ED1-positive monocytes, which were present to the same extent in pancreas tissue in AP + GSK180-treated rats (**Supplementary Fig. 7d**,**f**).

AP-MODS was associated with an acute rise in ALT, indicating hepatocyte injury, which was small in magnitude and equivalent in AP compared to AP + GSK180 treated rats; both groups of rats with AP became relatively hypoglycaemic compared to sham-operated controls, while serum albumin concentrations were only marginally affected (**Supplementary Fig. 7g**–**i**). An elevation in systemic IL-6 concentrations was seen in experimental AP, which was of lesser magnitude in rats with AP treated with GSK180 (**Supplementary Fig. 7j**). Interestingly, IL-10 concentrations were marginally but statistically significantly higher in AP rats and higher again in rats with AP treated with GSK180 (**Supplementary Fig. 7k**)

Acute lung injury (ALI) with features consistent with acute respiratory distress syndrome (ARDS) was observed on histological sections of lung tissue from rats with AP (**Fig. 4b** and **Supplementary Fig. 8a**–**c**). They also showed an increase in neutrophilic inflammation (**Fig. 4c**,**d**), lung protein leak (measured as

an increase in total protein concentration in bronchoalveolar fluid) (**Fig. 4e**), an increase in the circulating serum concentration of Krebs von den Lungen 6 (KL-6) (a type II pneumocyte MUC1-like glycoprotein and marker of incipient ALI in humans[15,16]) (**Fig. 4f**), and increased apoptosis (**Fig. 4g** and **Supplementary Fig. 8d**). All these features of ALI were essentially prevented by treatment with GSK180 ($[\text{total protein}]_{BAL}^{6h}$ in sham vs. AP vs. AP + GSK180 rats, 245 ± 18 mg/L vs. 332 ± 18 mg/L vs. 142 ± 6 mg/L, $P < 0.001$ one-way ANOVA across all groups, post hoc S-N-K threshold $P < 0.05$ significant between all groups, n = 7 to 8 rats per group; $[\text{KL-6}]_{serum}^{6h}$ in sham vs. AP vs. AP + GSK180 rats, 12 ± 1 ng/mL vs. 39 ± 3 ng/mL vs. 16 ± 2 ng/mL, $P < 0.001$ one-way ANOVA across all groups, post hoc S-N-K threshold $P < 0.05$ significant for sham vs. AP and AP vs. AP + GSK180, sham vs. AP + GSK180 n.s.; n = 7 to 8 per group; sham vs. AP vs. AP + GSK180 rats: 0.9 ± 0.2 vs. 3.3 ± 0.7 vs. 1.7 ± 0.4 TUNEL-positive cells/10^6 pixels; P=0.004 one-way ANOVA across all groups, post hoc S-N-K threshold $P < 0.05$ significant for sham vs. AP and AP vs. AP + GSK180, sham vs. AP + GSK180 n.s.; n = 7 to 8 rats per group (sham vs. AP vs. AP + GSK180 rats: 97 ± 20 vs. 180 ± 21 vs. 105 ± 70 MPO-positive cells/10^6 pixels; P=0.011 one-way ANOVA across all groups, post hoc S-N-K threshold $P < 0.05$ significant for sham vs. AP and AP vs. AP + GSK180, sham vs. AP + GSK180 n.s.; n = 7 to 8 rats per group). Interestingly, an infiltrating population of ED1-positive cells was present in lung tissue in both AP groups and significantly elevated in rats with AP treated with GSK180 (**Supplementary Fig. 8e**).

Experimentally-induced AP in rats resulted in a significant increase in TUNEL-positive renal tubular cells per unit area of tissue in the outer medullary stripe (the key anatomical region for acute tubular injury[17]) (**Fig. 4h**) (sham vs. AP vs. AP + GSK180 rats 1.3 ± 0.5 vs. 7.4 ± 1.3 vs. 2.1 ± 0.3 TUNEL-positive cells/10^6 pixels; $P < 0.001$ one-way ANOVA across all groups, post hoc S-N-K threshold $P < 0.05$ significant for sham vs. AP and AP vs. AP + GSK180, sham vs. AP + GSK180 n.s.; n = 7 to 8 rats per group). There was no evidence of histological damage (**Supplementary Fig. 9a–c**) or inflammatory infiltrate (**Supplementary Fig. 9d**) but in the rat model of AP we observed a significant loss of renal function as evidenced by elevated serum creatinine and urea at 6 hours after AP induction (**Fig. 4i,j**). Therapeutic administration of GSK180 in AP

protected against all aspects of this kidney injury ($[creatinine]_{serum}^{6h}$ in sham vs. AP vs. AP + GSK180 rats, 23 ± 2 mmol/L vs. 52 ± 8 mmol/L vs. 29 ± 5 mmol/L, P=0.007 one-way ANOVA across all groups, post hoc S-N-K threshold $P < 0.05$ significant for sham vs. AP and AP vs. AP + GSK180, sham vs. AP + GSK180 n.s.; $[urea]_{serum}^{6h}$ in sham vs. AP vs. AP + GSK180 rats, 8.2 ± 0.5 mmol/L vs. 13.4 ± 0.9 mmol/L vs. 10.7 ± 0.8 mmol/L, $P < 0.001$ one-way ANOVA across all groups, post hoc S-N-K threshold $P < 0.05$ significant between all groups; $n = 7$ to 8 rats per group). A modest but statistically significant increase in ED1-positive cell counts in the kidneys of rats with AP treated with GSK180 was observed (**Supplementary Fig. 9e**).

The development of MODS (and particularly ARDS) is a key determinant of outcome in critically ill individuals regardless of the initiating event[4]. AP serves as a paradigm for sterile systemic inflammation, and this work builds on a rapidly expanding body of work uncovering the potential role of the kynurenine pathway in several inflammatory and degenerative disease states, and is the first to demonstrate therapeutic efficacy of KMO inhibition to protect against MODS.

Increased tryptophan metabolism through the kynurenine pathway has been detected in systemic inflammation in humans during AP[6], trauma[18,19], coronary artery bypass surgery[20], sepsis[21], and chronic renal failure[22]. Oxidative stress and apoptotic cell death mediated by 3–hydroxykynurenine have been proposed as drivers of disease[23,22]. How 3–hydroxykynurenine results in tissue injury in AP is yet to be fully elucidated, but inference can be made from related experiments. In primary cultured neurons, 3–hydroxykynurenine causes cell death by apoptosis by producing reactive oxygen species including superoxide radicals and hydrogen peroxide (H_2O_2)[24,25], which can be counteracted by anti-oxidants[26] or blockade of intracellular peroxidase activity[24]. Furthermore, the oxidation product of 3–hydroxykynurenine itself, a short-lived quinone-imine, is highly reactive with the thiol and amine groups of proteins[27].

KMO inhibition increases plasma concentrations of kynurenic acid, which may be potentially protective and also harmful in the context of AP. Kynurenic acid activates the G-protein coupled receptor, GP35, and in doing so inhibits LPS-induced TNF release from human peripheral blood mononuclear cells[28]. In mice given a near-lethal dose of LPS, kynurenic acid administration prevents TNFα

release and reduces lethality[29]. kynurenic acid elevation during KMO blockade may also therefore contribute to the benefit seen in *Kmo*^{null} mice with AP and GSK180-treated rats with AP by exerting an anti-inflammatory effect on innate immune cells. Kynurenic acid elevates the seizure threshold of mice and rats given intracerebral quinolinic acid by potent antagonism at the glycine allosteric site of the NMDA receptor complex, and therefore a KMO inhibitor may be sedative.

The mechanisms leading to increased kynurenine pathway metabolites during sterile systemic inflammation are complex. Certainly it is clear that increased kynurenine substrate is made available through increased IDO activity in extra-hepatic tissues[30]. IDO is profoundly upregulated by bacterial lipopolysaccharide and pro-inflammatory cytokines, in particular IFNγ[30]. Furthermore, inflammation-induced tryptophan–2,3–dioxygenase activity resulting in increased levels of kynurenine regulates the induction of tolerance to lipopolysaccharide and is dependent on IDO1 activity[31]. These orthodox inflammatory signals also upregulate KMO activity in human monocytes[32] and monocyte-derived macrophages[33]. Human monocytes show increased gene expression of IDO1, KMO and QPRT (quinolinate phosphoribosyltransferase, a gene encoding an enzyme downstream in the kynurenine pathway) when incubated with IFNγ, and KMO expression correlates with kynurenine pathway activation measured by the tryptophan:kynurenine ratio[34]. Interleukin-1β (IL-1β) is also reported to drive upregulated KMO mRNA expression[35]. Interestingly, the induction of IDO expression *in vitro* in response to the toll-like receptor agonists LPS and CpG has been shown to be dependent on the presence of a functioning aryl hydrocarbon receptor (AhR) complex[36,37]. Furthermore, kynurenine is now regarded as a potent AhR ligand and together this complex is a key mechanistic contributor to endotoxin tolerance[31,38]. Exogenous kynurenine added in co-culture of dendritic cells with T-lymphocytes rescues a type 1 T-regulatory phenotype, limits Th17 cell induction and reduces Th17 cytokine release in an AhR-null system when compared to AhR-competent co-cultures[36]. This is congruent with the observation that the presence of kynurenine during CD3/CD28 antibody-induced T-cell proliferation decreases overall proliferation[38] and increases the proportion of FoxP3^{+} T-regulatory cells

generated[37]. It is possible, although yet to be explicitly defined, that these adaptive immune-cell mediated mechanisms may contribute to the efficacy of KMO inhibition shown in our experiments. Furthermore, the increase in kynurenine as a consequence of KMO inhibition may also contribute to free-radical scavenging. Experimentally, addition of kynurenine scavenges hydrogen peroxide and, to a lesser extent, superoxide radical, and has a concentration-dependent inhibitory effect on the production of reactive oxygen species by activated neutrophils, without directly affecting NADPH oxidase function or phagocytosis[39].

In *Kmo*^{null} mice, fecundity, fertility and longevity up to 2 years of age are not affected, from which we can infer that prolonged KMO blockade with consequent chronic exposure to significantly elevated concentrations of kynurenic acid and kynurenine is well tolerated, at least in adapted mice. Independently, a second *Kmo*^{null} mouse strain has been generated by others[40], which has an identical biochemical phenotype to the *Kmo*^{null} mouse strain generated by iKOMP and us. Together, the clear biochemical phenotypic changes in these two independently generated *Kmo*^{null} mice strains demonstrate unequivocally that KMO activity defines the metabolic fate of kynurenine.

GSK180 is a potent inhibitor of isolated KMO, but is less potent in the cellular context. The passive permeability of GSK180 across an artificial membrane was measured and found to be extremely low ($< 3 \times 10^{-6}$ cms^{-1}, $n = 3$) and measurement of drug concentration confirms that the intracellular level is more than 30 times lower than the extracellular concentration. It therefore seems reasonable to conclude that the lower potency observed in the cell-based assay is based on poor access of the compound into the intracellular compartment, necessitating higher drug levels to show pharmacodynamic activity. This leads to the unwanted (non-KMO mediated) effects on tryptophan and kynurenic acid but, used carefully, GSK180 remains a useful tool to probe the therapeutic potential of KMO inhibition. Improving cell potency will be a key component of the search for a clinical candidate.

AP-MODS is an early event in the overall disease course of AP, occurring in the first few hours to days after the onset of symptoms[3,9]. If we are to rationalize KMO activity as a key contributor to AP-MODS, tryptophan and kynurenine

metabolism must be rapid and occur within the expected timeframe of onset of AP-MODS. The rate of change in metabolite levels following administration of GSK180 strongly support this, and provide convincing evidence that kynurenine metabolism occurs within a disease-relevant time course and that tryptophan is continuously metabolized and replenished to the plasma compartment on a large scale. Importantly, this rate of metabolic flux is well within the proposed timescale of tryptophan metabolism via KMO as an important and early contributory mechanism in AP-MODS. In addition, because KMO inhibition protects against extrapancreatic organ injury without a need to diminish the severity of the initiating pancreatic tissue damage, the clinical applicability is enhanced.

In conclusion, our experiments demonstrate a novel contributory metabolic mechanism of remote organ injury triggered by sterile initiators of systemic inflammation. Moreover, we have also shown that the metabolic target, KMO, is susceptible to therapeutic blockade. Together, these data strongly support a therapeutic role for KMO inhibitors in critical illness. Our findings therefore establish KMO inhibition as a novel therapeutic strategy in AP-MODS and possibly other severe acute systemic inflammation.

Accession codes

The final model of the crystal structure presented in **Figure 3d** has been deposited in the Protein Data Bank under the accession code 5fn0.

Acknowledgments

DJM is supported by a Clinician Scientist Fellowship from the Health Foundation/Academy of Medical Sciences, the Medical Research Council Developmental Pathway Funding Stream and Wellcome Trust Institutional Strategic Support Fund. JPI acknowledges the support of the Medical Research Council. We thank D. Harbison, Edinburgh Bioquarter, the staff of the Central Bioresearch Services, University of Edinburgh; F. Howie, D. Mauchline, M. McMillan, L. Boswell, M. Millar; colleagues in the Medical Research Council Centre for Inflammation Research for support and advice.

Author contributions

DJM, SPW, IU and JL led the University of Edinburgh/GlaxoSmithKline Discovery Partnership with Academia collaboration. DJM, SPW, IU, OJG, JH, SEMH, DH, JL and JPI developed and refined the hypothesis and experimental design. DJM, XZ, IU, BB, NA, LT and VB did or designed the *in vivo* experiments. XZ, MGFS and DJM made the genetically-altered mice from iKOMP ES cells. JEB reported the pathology. SPW, IU, JL, MB and KW did or designed the cell based experiments. NZMH, SPW and MB did or developed the LC-MS/MS. JPH, CH, JL, SPW, DJM, AM, IU and DH did or designed assay development and screening. OM, AW, JL, DH did or designed the medicinal chemistry. PR, CGM and MW, did the structural biology. All authors contributed to data analysis or interpretation. All authors contributed to, revised and approved the final version of the manuscript.

References

1. Lowenfels, A.B., Maisonneuve, P. & Sullivan, T. The changing character of acute pancreatitis: epidemiology, etiology, and prognosis. *Curr Gastroenterol Rep* **11**, 97-103 (2009).

2. Pastor, C.M., Matthay, M.A. & Frossard, J.L. Pancreatitis-associated acute lung injury: new insights. *Chest* **124**, 2341-2351 (2003).

3. McKay, C.J. & Buter, A. Natural history of organ failure in acute pancreatitis. *Pancreatology* **3**, 111-114 (2003).

4. Skouras, C.*, et al.* Early organ dysfunction affects long-term survival in acute pancreatitis patients. *HPB (Oxford)* (2014).

5. Vécsei, L., Szalárdy, L., Fülöp, F. & Toldi, J. Kynurenines in the CNS: recent advances and new questions. *Nat Rev Drug Discov* **12**, 64-82 (2013).

6. Mole, D.J.*, et al.* Tryptophan catabolites in mesenteric lymph may contribute to pancreatitis-associated organ failure. *Br J Surg* **95**, 855-867 (2008).

7. Nakagami, Y., Saito, H. & Katsuki, H. 3-Hydroxykynurenine toxicity on the rat striatum in vivo. *Jpn J Pharmacol* **71**, 183-186 (1996).

8. Zhang, H.*, et al.* IL-6 trans-signaling promotes pancreatitis-associated lung injury and lethality. *J Clin Invest* **123**, 1019-1031 (2013).

9. Mole, D.J., Olabi, B., Robinson, V., Garden, O.J. & Parks, R.W. Incidence of individual organ dysfunction in fatal acute pancreatitis: analysis of 1024 death records. *HPB (Oxford)* **11**, 166-170 (2009).

10. Zwilling, D.*, et al.* Kynurenine 3-monooxygenase inhibition in blood ameliorates neurodegeneration. *Cell* **145**, 863-874 (2011).

11. Courtney, S. & Scheel, A. Modulation of the kynurenine pathway for the potential treatment of neurodegenerative diseases. *Topics in Medicinal Chemistry* **6**, 149-176 (2010).

12. Lowe, D.M.*, et al.* Lead Discovery for Human Kynurenine 3-Monooxygenase by High-Throughput RapidFire Mass Spectrometry. *J Biomol Screen* **19**, 508-515 (2014).

13. Amaral, M.*, et al.* Structural basis of kynurenine 3-monooxygenase inhibition. *Nature* **496**, 382-385 (2013).

14. McArthur, J.N. & Dawkins, P.D. The effect of sodium salicylate on the binding of L-tryptophan to serum proteins. *J Pharm Pharmacol* **21**, 744-750 (1969).

15. Sato, H.*, et al.* KL-6 levels are elevated in plasma from patients with acute respiratory distress syndrome. *Eur Respir J* **23**, 142-145 (2004).

16. Nathani, N.*, et al.* Kerbs von Lungren 6 antigen is a marker of alveolar inflammation but not of infection in patients with acute respiratory distress syndrome. *Crit Care* **12**, R12 (2008).

17. Kipari, T.*, et al.* Nitric oxide is an important mediator of renal tubular epithelial cell death in vitro and in murine experimental hydronephrosis. *Am J Pathol* **169**, 388-399 (2006).

18. Logters, T.T.*, et al.* Increased plasma kynurenine values and kynurenine-tryptophan ratios after major trauma are early indicators for the development of sepsis. *Shock* **32**, 29-34 (2009).

19. Pellegrin, K.*, et al.* Enhanced enzymatic degradation of tryptophan by indoleamine 2,3-dioxygenase contributes to the tryptophan-deficient state seen after major trauma. *Shock* **23**, 209-215 (2005).

20. Forrest, C.M.*, et al.* Kynurenine metabolism predicts cognitive function in patients following cardiac bypass and thoracic surgery. *J Neurochem* **119**, 136-152 (2011).

21. Wang, Y.*, et al.* Kynurenine is an endothelium-derived relaxing factor produced during inflammation. *Nat Med* **16**, 279-285 (2010).

22. Pawlak, K., Domaniewski, T., Mysliwiec, M. & Pawlak, D. The kynurenines are associated with oxidative stress, inflammation and the prevalence of cardiovascular disease in patients with end-stage renal disease. *Atherosclerosis* **204**, 309-314 (2009).

23. Wang, Q.*, et al.* Activation of NAD(P)H oxidase by tryptophan-derived 3-hydroxykynurenine accelerates endothelial apoptosis and dysfunction in vivo. *Circ Res* **114**, 480-492 (2014).

24. Eastman, C.L. & Guilarte, T.R. The role of hydrogen peroxide in the in vitro cytotoxicity of 3-hydroxykynurenine. *Neurochem Res* **15**, 1101-1107 (1990).

25. Okuda, S., Nishiyama, N., Saito, H. & Katsuki, H. Hydrogen peroxide-mediated neuronal cell death induced by an endogenous neurotoxin, 3-hydroxykynurenine. *Proc Natl Acad Sci U S A* **93**, 12553-12558 (1996).

26. Okuda, S., Nishiyama, N., Saito, H. & Katsuki, H. 3-Hydroxykynurenine, an endogenous oxidative stress generator, causes neuronal cell death with apoptotic features and region selectivity. *J Neurochem* **70**, 299-307 (1998).

27. Giles, G.I., Collins, C.A., Stone, T.W. & Jacob, C. Electrochemical and in vitro evaluation of the redox-properties of kynurenine species. *Biochem Biophys Res Commun* **300**, 719-724 (2003).

28. Wang, J.*, et al.* Kynurenic acid as a ligand for orphan G protein-coupled receptor GPR35. *J Biol Chem* **281**, 22021-22028 (2006).

29. Moroni, F., Cozzi, A., Sili, M. & Mannaioni, G. Kynurenic acid: a metabolite with multiple actions and multiple targets in brain and periphery. *J Neural Transm* **119**, 133-139 (2012).

30. Murakami, Y. & Saito, K. Species and cell types difference in tryptophan metabolism. *Int J Tryptophan Res* **6**, 47-54 (2013).

31. Bessede, A.*, et al.* Aryl hydrocarbon receptor control of a disease tolerance defence pathway. *Nature* **511**, 184-190 (2014).

32. von Bubnoff, D.*, et al.* FcepsilonRI induces the tryptophan degradation pathway involved in regulating T cell responses. *J Immunol* **169**, 1810-1816 (2002).

33. Chiarugi, A., Calvani, M., Meli, E., Traggiai, E. & Moroni, F. Synthesis and release of neurotoxic kynurenine metabolites by human monocyte-derived macrophages. *J Neuroimmunol* **120**, 190-198 (2001).

34. Jones, S.P.*, et al.* Expression of the Kynurenine Pathway in Human Peripheral Blood Mononuclear Cells: Implications for Inflammatory and Neurodegenerative Disease. *PLoS One* **10**, e0131389 (2015).

35. Zunszain, P.A.*, et al.* Interleukin-1β: a new regulator of the kynurenine pathway affecting human hippocampal neurogenesis. *Neuropsychopharmacology* **37**, 939-949 (2012).

36. Nguyen, N.T.*, et al.* Aryl hydrocarbon receptor negatively regulates dendritic cell immunogenicity via a kynurenine-dependent mechanism. *Proc Natl Acad Sci U S A* **107**, 19961-19966 (2010).

37. Mezrich, J.D.*, et al.* An interaction between kynurenine and the aryl hydrocarbon receptor can generate regulatory T cells. *J Immunol* **185**, 3190-3198 (2010).

38. Opitz, C.A.*, et al.* An endogenous tumour-promoting ligand of the human aryl hydrocarbon receptor. *Nature* **478**, 197-203 (2011).

39. Genestet, C.*, et al.* Scavenging of reactive oxygen species by tryptophan metabolites helps Pseudomonas aeruginosa escape neutrophil killing. *Free Radic Biol Med* **73**, 400-410 (2014).

40. Giorgini, F.*, et al.* Targeted deletion of kynurenine 3-monooxygenase in mice: a new tool for studying kynurenine pathway metabolism in periphery and brain. *J Biol Chem* **288**, 36554-36566 (2013).

Figure legends

Figure 1. The kynurenine pathway of tryptophan metabolism (**a**) Diagram of the kynurenine pathway. (**b**–**g**) *Kmo*^{null} mouse steady state kynurenine metabolite serum concentrations. Graphs show individual data with horizontal lines showing mean ± s.e.m. BLQ = below limit of quantitation. Dashed line (---) shows LQ for 3–hydroxykynurenine. *P < 0.05 by independent samples t-test (two-sided), n = 5 mice per group. All mice were male. For panel **d**, values that were BLQ were assigned the LQ value to allow statistical analysis.

Figure 2. *Kmo*^{null} mice are protected against lung, liver and kidney injury during experimental AP. (**a**) Composite histological pancreas injury score. (**b**) Representative lung tissue photomicrographs (haematoxylin and eosin stain) from *Kmo*^{wt} mice with AP (n = 7) show lung injury manifested as thickening of alveolar walls with vascular congestion (black arrow), interstitial oedema (white arrow) and inflammatory cell infiltrates (blue arrow) compared to lung tissue from sham control *Kmo*^{wt} mice (n = 7) and sham control *Kmo*^{null} mice (n = 6). This pathology is less marked in lung tissue from *Kmo*^{null} mice with AP (n = 7). Scale bar, 300 μm. (**c**) Lung neutrophil infiltration in response to AP. Representative immunohistochemistry images show neutrophil infiltration (MPO$^+$ cells, brown-stained, white arrow) into lung tissue from AP mice but not sham control mice. Scale bar, 300 μm. Group sizes as for panel **b** (**d**) Apoptotic TUNEL$^+$ cell counts in lung tissue. (**e**) Apoptotic TUNEL$^+$ cell counts in kidney tissue. (**f**) Serum alanine aminotransferase (ALT) concentrations. (**g**) Serum creatinine concentrations. **All panels**: Data are plotted for individual mice with horizontal lines showing mean ± s.e.m. *P < 0.05, **P < 0.01 and ***P < 0.001 by ANOVA with *post hoc* Student-Newman-Keuls homogeneous subset analysis (subset for α = 0.05); N.S. = not significant. For panels **f** and **g**, for *Kmo*^{null} mice with AP, the group size is (n = 5) due to blood sampling failure in 2 mice.

Figure 3. Discovery of the KMO inhibitor GSK180. (**a**) Kynurenine cyclization strategy that led to the discovery of GSK180. (**b**) Indicative dose-response inhibition plots of GSK180 vs. human KMO expressed in insect cell lysates,

human and rat KMO expressed in intact HEK293 cells and human primary hepatocytes. (**c**) Pharmacokinetic/pharmacodynamic profile of GSK180 in rat administered as an i.v. bolus. Plasma levels of drug and concentrations of kynurenine and kynurenic acid are shown. Data are mean ± s.d. of *n* = 3 rats. (**d**) Crystal structure of KMO in complex with the inhibitor. Enzyme residues (grey) surrounding the bound inhibitor (cyan) are shown in stick representation, with hydrogen bonds shown as dashed lines (magenta). Heteroatoms are colored according to atom type: nitrogen (blue), oxygen (red), sulphur (yellow) and chlorine (green).

Figure 4. Therapeutic administration of GSK180 protects against lung, liver and kidney injury during experimental AP in rats. (**a**) Composite histological pancreas injury score. (**b**) Representative photomicrographs of lung tissue stained with haematoxylin and eosin shows secondary lung injury in untreated rats with AP (*n* = 7) compared to sham control rats (*n* = 8) and GSK180-treated rats with AP (*n* = 7) manifested as alveolar wall thickening (white arrow), inflammatory cell infiltration (black arrow) and vascular congestion (blue arrow). Scale bar, 300 μm. (**c**) Lung neutrophil infiltration in experimental AP. Representative immunohistochemistry images show neutrophil infiltration (MPO^+ cells, brown-stained, white arrow) into lung tissue from AP rats (*n* = 7) but not sham control rats (*n* = 8). GSK180 treated rats (*n* = 7) have reduced lung neutrophil infiltration. Scale bar, 300 μm. (**d**) Enumeration of MPO^+ cells/10^6 pixels in lung tissue. (**e**) Lung bronchoalveolar lavage protein concentration. (**f**) Serum concentrations of the glycoprotein lung injury biomarker Krebs von den Lungen-6 (KL-6) (**g**) Enumeration of $TUNEL^+$ cells/10^6 pixels in lung tissue (**h**) Enumeration of $TUNEL^+$ cells/10^6 pixels in kidney tissue. (**i**) Serum creatinine concentrations. (**j**) Serum urea concentrations. **All panels**: Group sizes were: sham *n* = 8, AP *n* = 7 and AP + GSK180 *n* = 7 rats. Unless otherwise stated, data are plotted for individual rats with horizontal lines show mean ± s.e.m. $*P < 0.05$, $**P < 0.01$ and $***P < 0.001$ by ANOVA with *post hoc* Student-Newman-Keuls homogeneous subset analysis (subset for $\alpha = 0.05$); N.S. = not significant.

Online methods

Ethical approvals

All experiments involving the use of animals were reviewed and approved by the University of Edinburgh Ethical Review Committee and performed under license in accordance with the United Kingdom Animals (Scientific Procedures) Act 1986 and compliant with the GlaxoSmithKline Policy on the Care, Welfare and Treatment of Animals.

Generation of *Kmo*^{null} mice

Embryonic stem cells (JM8.N4, C57BL/6N background) in which the fourth intron of *Kmo* has been targeted by a 'knockout-first' approach were obtained from the International Knockout Mouse Project[41] (KOMP) and microinjected into mouse blastocysts derived from albino C57BL/6J-*Tyr*$^{c-2J}$ mice prior to implantation into pseudopregnant foster dams. Litters containing chimeras were born which were backcrossed onto the C57BL/6J-*Tyr*$^{c-2J}$ line and offspring carriers of the transgene were selected on the basis of black coat colour followed by genotyping to be used as founders. These founders were backcrossed to C57BL/6J to generate a strain heterozygote (*Kmo*$^{tm1a(KOMP)Wtsi}$) for the transgene to establish a breeding colony. Mice were backcrossed for at least 6 generations and subsequently bred as heterozygous pairs to generate mice homozygous for the transgene (referred to as *Kmo*^{null}) and wild type (*Kmo*^{wt}) littermate controls. To revert to a functional KMO biochemical phenotype, *Kmo*^{null} mice were crossed with the *Flp*-deleter *C57BL/6-Tg(CAG-Flpe)2Arte* to excise the promoter-driven cassette. These mice were subsequently bred as heterozygous pairs to generate mice homozygous for the loxP-flanked lacZ-deleted transgene (*Kmo*$^{tm1c(KOMP)Wtsi/flox(ex5)}$, referred to as *Kmo*$^{FRT\text{-}deleted}$), and non-transgene controls (*Kmo*$^{flpe\text{-}wt}$) on the correct background strain. All mouse genotypes were confirmed by standard PCR-based genotyping of genomic DNA isolated from ear clips. The following primer sequences were used for PCR genotyping: LacZ: 5'-GAGTTGCGTGACTACCTACGG-3' and 5'-GTACCACAGCGGATGGTTCGG-3' to yield a single PCR product of 453 base pairs representing the targeted *Kmo*$^{tm1a(KOMP)Wtsi}$ allele. *Kmo* primers: 5'-GCATTAAAGGACAGTCAACCTG-3' and 5'-

CACTGGACTGTGAGTGCTTG-3' to generate an 830 base pair band representing the non-targeted *Kmo* allele, or no band representing the recombined *Kmo* allele.

Kmo mRNA tissue expression

We made cDNA using a Quantitect kit applied to RNA extracts of tissue made using microRNAEasy kits (Qiagen). We used inventoried TaqMan assays for mouse *Kmo* in a standard TaqMan FAST Assay with amplification detected on an AB7500 FAST cycler (Applied Biosystems). We performed all assays as duplex reactions with an endogenous 18S RNA internal control.

LC-MS/MS analysis of tryptophan metabolites

Samples of serum, plasma, lysate or tissue homogenate were diluted to a ratio of 2:5 in 5 mM ammonium formate containing 0.1% trifluoracetic acid. Protein was precipitated by the addition of ice-cold 100% trichloroacetic acid, samples incubated for 30 minutes at 4 °C and centrifuged to obtain the supernatant. Serial dilutions of each tryptophan metabolite were prepared over appropriate concentration ranges to prepare a calibration curve to permit quantitation. 10µL volumes of each sample were injected onto a Waters XSelect HSS PFP column (2.5 µm; 100 × 3 mm internal diameter, Waters, Elstree, Herts., UK) using a Waters Acquity UPLC autosampler, coupled to an ABSciex QTRAP 5500 mass spectrometer. The flow rate was 0.35 mL/min at 25 °C**.** Separation was carried out using a A – water, B – methanol gradient (both containing 0.1% formic acid). Conditions were 50% to 60% B over 60 seconds, 65% to 35% B over 180 seconds, hold 65% B for 110 seconds, 65% to 50% B over 10 seconds and requilibration at 50% B for 200 seconds. The total run time was 10 minutes. The mass spectrometer was operated in positive ion electrospray mode. The transitions for the protonated analytes were kynurenine (*m/z* 209-192), 3–hydroxykynurenine (*m/z* 225-202), tryptophan (*m/z* 205-188), kynurenic acid (*m/z* 190-144), 3HAA (*m/z* 154-136), d5-tryptophan (*m/z* 210-122), d4-kynurenine (*m/z* 213-150), d4-kynurenic acid (*m/z* 194-148), d3-3–hydroxykynurenine*(m/z* 228-165) and d3-HAA(*m/z* 157-139). Collision energies were 29, 15, 11, 31, 33, 37 29, 31, 17 and 31 V respectively. Data was acquired and processed using Analyst 3.0 software (ABI Sciex).

KMO tissue activity assay

To assay for KMO activity mouse liver tissue (100 mg) was homogenized in 1 ml 0.32 µM sucrose solution, centrifuged and the supernatant removed. Total protein concentration was evaluated using the Pierce BCA kit. A final concentration of 200 µg/ml total protein was added to a master mix containing 200µM kynurenine, 800µM NADP, 3 mM G-6-P, 1 unit G6PD, 4 mM $MgCl_2$ and 2 mM HEPES pH 7.4 and incubated for 2 h at 37 °C at 200 rpm on an orbital shaker. Assays were terminated by addition of 500 µl acetonitrile, 250 ng/ml d5-tryptophan, dried down at 65 °C under nitrogen then re-solubilized in 100 µl 70:30 water:methanol prior to LC-MS/MS analysis. Separation of 3–hydroxykynurenine was carried out as described for the cellular KMO enzyme inhibition assay.

Experimental acute pancreatitis

To induce experimental AP in mice we adapted an existing model[42]. Briefly, male mice aged 20 ± 1 weeks (mean ± s.e.m., no age difference between experimental groups) from our transgenic breeding colony (housed in groups in 12-hour light cycles with free access to standard chow and water) were anaesthetized with inhaled isoflurane induction followed by i.p. metomidate and ketamine, using s.c. buprenorphine analgesia to allow laparotomy and retrograde intraductal injection of 100 µl of 5% sodium taurocholate, followed by i.p. bolus deposition of caerulein (30 µg/kg in 500 µl 0.9% saline). Sham-operated control mice underwent anaesthesia, laparotomy and i.p. deposition of 500 µl 0.9% saline. Mice were recovered in a warm area and housed singly for the duration of the experiment. At euthanasia, mice were re-anaesthetised with isoflurane and rapidly exsanguinated by direct cardiac puncture prior to tissue sampling into 10% buffered formalin or liquid nitrogen as appropriate. In exploratory phenotyping studies, mice were given 1 mg/kg deuterated d_5-tryptophan i.v. 1 hour before euthanasia.

To induce experimental AP in rats, we used our variation[43] of the combined model of AP in rats described in detail elsewhere[44]. Briefly, male Sprague-Dawley outbred rats aged 8 to 12 weeks (Harlan Inc., UK) housed in groups in 12-hour light cycles were allowed free access to standard chow and

water and acclimated for greater than 7 days after delivery. We placed carotid arterial and jugular venous cannulas under general anaesthetic without recovery using inhaled isoflurane with oxygen and analgesia using buprenorphine s.c.. At laparotomy, we gave a 10-minute pressure-controlled retrograde biliopancreatic infusion of 10 mM glycodeoxycholic acid in glycyl-glycine buffer pH 8.0. This was followed by supramaximal pancreatic stimulation by a 6h infusion of caerulein (Sigma) at 5 μg/kg/hour. For exploratory studies of tryptophan dynamics we administered 1 mg/kg deuterated d_5-tryptophan i.v. 1 hour before euthanasia in all groups of rats although this data is not reported here. As we have previously reported[45], this model results in amylasemia, histological acute pancreatitis with necrosis, haemoconcentration and metabolic acidosis, with a systemic inflammatory response including pyrexia and tachypnoea. We retrieved tissues into 10% buffered formalin or liquid nitrogen as appropriate. Amylase, albumin, ALT, glucose, urea and creatinine were analyzed in serum extracts utilising commercial kits (Alpha Laboratories Ltd. Eastleigh, UK) adapted for use on a Cobas Fara centrifugal analyzer (Roche Diagnostics Ltd, Welwyn Garden City, UK). Pancreatic edema (graded 0-3), inflammatory cell infiltrate (graded 0-3) and acinar cell necrosis (graded 0-3) were scored in an observer-blind fashion according to the system previously reported[46]. Mouse cytokines were analyzed using Mouse ProInflammatory 7-Plex Ultra-Sensitive Kit (IL-1β, IL-12p70, IFNγ, IL-6, KC/GRO, IL-10 and TNFα) according to the manufacturers protocols (Meso Scale Discovery, Gaithersburg, MD, USA). Imaging of the plate was performed using a Sector 2400 Imager (Meso Scale Discovery, Gaithersburg, MD, USA). A standard curve for each analyte was curve-fitted, allowing determination of the concentration in pg cytokine per ml. Rat cytokines were analyzed using a Rat Fluorokine MAP Base Luminex Performance Assay cytokine kit with IFNγ, IL-10, L-selectin/CD62L, IL-18/IL-1F4, TNF-alpha, IL-1β/IL-1F2 and IL-6 individual bead sets, according to the manufacturer's protocol (R&D Systems, MN, USA). The level of fluorescence of the cytokine-specific beads was analyzed using Bio-Rad Bio-Plex 200 system (BioRad, CA, USA). Cytokine concentrations were determined based on a standard curve included in each plate, using cytokine standards provided by the manufacturer.

Histology and digital image analysis

Sections (3μm) of formalin-fixed paraffin embedded tissue were de-waxed and taken through a decreasing series of graded alcohols to water. Haematoxylin and eosin staining were performed according to standard protocols. Haematoxylin and eosin stained pancreas and kidney sections were scored in a blinded fashion by a pathologist using previously published parameters[46,47]. We assayed TUNEL using a DeadEnd™ Fluorometric or Colorimetric Kits (Promega Inc.) according to the manufacturer's protocol. Immunohistochemistry was done according to standard protocols. The following primary antibodies were used: anti-mouse F4/80 BM8 antibody #14-4801 (eBioscience, Hatfield, UK) at 1:100 dilution; rabbit anti-MPO polyclonal antibody #1224 (Merck Millipore Corporation) at 1:1,000 dilution for both rat and mouse MPO; mouse anti-rat CD68 (ED-1) monoclonal antibody MCA 341R (AbD Serotec) at 1:200 dilution. Visualisation was with diaminobenzoate (DAB) according to standard protocols. Immunohistochemistry slides were scanned in their entirety using an Axio Scan.Z1 system (Zeiss microscopy GmbH, Oberkochen, Germany) and stored as .czi files before export as reduced sized .jpg files into ImageJ.

For mouse lung and kidney TUNEL enumeration, three representative 100× magnification fields were sampled directly using a fluorescence microscope Zeiss Axioskop2 with AxioCamMR3, captured with Axiovision software, or in a second imaging batch using a stereologer microscope Nikon Eclipse E800 captured with ImagePro software, then exported as .jpg or .tif files. No formal investigator blinding was performed. In order to allow comparison of images from both imaging batches, three areas equivalent to a 100× image of each composite tile-scanned image were sampled from the entire section and exported as .jpg or .tif. Images were imported into ImageJ and TUNEL positive cells were enumerated. For lung tissue, TUNEL positive cells were expressed per unit tissue area, where the tissue area was determined by applying the following settings in ImageJ: RGB split file, green channel, adjust threshold manually according to the threshold intensity histogram and screen image to include all tissue, then running the Measure macro in ImageJ. For kidney TUNEL analysis in mice, the denominator tissue area was the sampled field in 10^6 pixels. The average score of 3 fields per section was given as the score for that animal.

For rat lung TUNEL enumeration, the entire available area of the tile-scanned lung section (excluding the pleural surface which was deselected manually) was analyzed using the cell count algorithm, applying the following settings: RGB split file, threshold 170/255 on green channel, circularity 0-1.0, size 20-10,000 pixel^2. For rat kidney sections, the entire outer medullary stripe available for each tiled image was selected manually and analyzed using the cell count algorithm. No formal investigator blinding was performed. Background tissue areas for the denominator were determined as described for mice.

Enumeration of MPO^+, $F4/80^+$ and $ED1^+$ cells was done using ImageJ and expressed as positive cells per million pixels. For lung and kidney tissue, counts were expressed per unit area of tissue. For pancreas tissue, because many infiltrating inflammatory cells occupy the spaces between pancreatic acinar cells and lobules, immunopositive cell counts are expressed per unit area of the measured field. For mouse F4/80 counts in lung and kidney, the ImageJ algorithm was not able to accurately detect the cells due to a combination of shape and low staining intensity. Therefore, the cells were counted manually, without routine observer blinding. For those tissues undergoing manual cell counts, areas for the denominator were possible to be automatically determined in ImageJ, after thresholding to detect all tissue. After any quantitative analysis and for publication figure presentation only, immunohistochemistry images were uniformly processed across the entire image using Mac OS X Preview >Adjust color.

In vitro KMO inhibition assay

Inhibition of KMO activity was determined as previously described[12]. Briefly, full length human *KMO* was expressed as a GST fusion in Sf9 cells (obtained from EACC, catalogue number 89070101; tested for mycoplasma according to the ATCC Universal Mycoplasma detection protocol, catalogue number 30-1012K when each vial was drawn for propagation) and used as a membrane suspension. Reactions were run at saturating NADPH (200 µM) and around K_M for kynurenine (10 µM) in a buffer of 50 mM Hepes (pH 7.5), 2 mM DTT, 1 mM EDTA, 100 µM Chaps and stopped after 2 hours by addition of TFA. Plates were read on a RapidFire 200 autosampler/solid-phase extraction system (Agilent Technologies) coupled to a Sciex API4000 triple quadrupole mass spectrometer (Applied Biosystems) operated in positive ion mode. Multiple reaction monitoring was used to detect both kynurenine and 3–hydroxykynurenine.

Cellular KMO enzyme inhibition assay

Full length human *KMO* (GenBank Accession No. NM_003679) was prepared as a synthetic gene (GenScript) and ligated into pcDNA5/FRT/V5-His-TOPO (Invitrogen). HEK293 cells (Flp-In™-293 cells, Invitrogen) were co-transfected with the resulting recombinant KMO vector and pOG55 (Invitrogen) and grown in the presence of hygromycin to generate the stable HEK293-*huKMO* cell line. The authenticity of each stable HEK293 cell line was confirmed by STR profiling (Identicell, Denmark). HEK293-*huKMO* cells were grown in 96-well microplate in DMEM medium containing 1% glutamine, 1% penicillin/streptomycin and incubated in 5% CO_2, 95% O_2 at 37 °C. Serial dilutions of compound were prepared in 10% DMSO from a 10 mM stock solution in 100% DMSO. In a V-bottomed microplate, GSK180 at an appropriate concentration was added in duplicate at up to 10 different concentrations. For low inhibition controls, 1% DMSO was added to the microplate and for high inhibition controls, 10 mM 6-(3,4-dichlorophenyl)pyrimidine-4-carboxylic acid (CAS Number 1207723-55-4) was added. The medium from the cells was removed and a solution of Opti-MEM medium containing 1% glutamine, 1% penicillin/streptomycin and 200 µM L-kynurenine was added to the compound and control wells and incubated in 5% CO_2, 95% O_2 at 37 °C for 20 hours. Following incubation, the medium was

transferred to a deep well block containing acetonitrile and d5-tryptophan, centrifuged at 4 °C to remove debris and dried under nitrogen at 65 °C for 1h hour. Residues were resuspended in water/methanol (70:30) prior to LC-MS/MS analysis. LC-MS/MS analysis was carried out on a TSQ Quantum Discovery Triple Quadrupole Mass Spectrometer (ThermoFisher) coupled to an Aria CTC Autosampler and HPLC system (ThermoFisher). Separation was carried out on an Allure Biphenyl column at 50 °C using a water/methanol gradient (30% to 70% methanol over 30 s, held at 70% methanol for 60 s, then returned to 30% methanol over 120 s and re-equilibrated at 30% methanol for 60 s). The peak area ratio for 3–hydroxykynurenine/d5-tryptophan was used to determine the percentage inhibition. Data were fitted to the 4-parameter logistic equation (Y=Bottom + (Top-Bottom)/(1+10^((LogEC$_{50}$-X)*HillSlope))) using GraphPad Prism software.

Freshly prepared human primary hepatocytes (Biopredict, Fr) were incubated overnight with compounds diluted in Williams' E basal media (Invitrogen) containing 10% FBS, 100 nM dexamethasone and 400 µM L-tryptophan (Sigma). Following incubation LC-MS/MS analysis was carried out on cell supernatant in order to detect and quantify metabolites. For presentation, the percentage inhibition was calculated using the observed increase in kynurenine, normalized to 100%. Data were fitted to the 4-parameter logistic equation (Y=Bottom + (Top-Bottom)/(1+10^((LogEC$_{50}$-X)*HillSlope))) using GraphPad Prism software

Cellular K_m determination

HEK293 cells stably transfected with either human KMO or rat *Kmo* were plated at 2×10^4 cells per well in 96-well poly-D-lysine-coated 96-well flat-bottomed microplates. Opti-MEM medium containing 1% glutamine, 1% penicillin/streptomycin and supplemented with varying concentrations of L-kynurenine (0 – 2,000 µM) was added and the cells incubated in 5% CO_2, 95% O_2 at 37 °C for between 8 and 20 hours such that turnover was less than 15% across all concentrations. Each concentration of L-kynurenine was added in duplicate. The cell supernatants were removed and analysed by LC-MS/MS to determine the amount of 3–hydroxykynurenine generated. The mean data for each

independent experiment were fitted to the Michaelis-Menten equation ($Y = V_{max} \times X/(K_m + X)$) using GraphPad Prism software.

Tryptophan pathway inhibition assays

Synthetic genes for full length human kynureninase (KYNU) and kynurenine amino transferase types 1 and 2 (KATI and KATII) were generated and ligated into the vector pET24b such that C-terminal six histidine tagged proteins were expressed in the *E. coli* strain BL21(DE3)pLysS. For KATI and KATII, *E. coli* were grown to OD600=0.6 at 37 °C with shaking and induced with 0.1 mM IPTG for 4 hours. For KYNU, *E. coli* were grown in ZYP-5052 auto-induction media[48] at 37 °C for 20 hours. Cells were harvested and lysed by sonication. N-laurylsarcosine was added to the KATII cell lysate to final concentration of 2% v/v, and mixed by vortexing. Cell free extracts were prepared by ultracentrifugation. KATI, KATII and KYNU were affinity purified on a 1 ml HisTrap FF column using a 0-1M imidazole gradient over 20 column volumes. KATI and KATII were further purified by anion exchange on a 1 ml HiTrap Q FF column, with a 0-1M NaCl gradient over 20 column volumes.

For KATI and KATII, a stopped fluorescence assay based on the method of Wong et al[49] was developed in 96-well format, using 1 mM sodium pyruvate and 90μM L-kynurenine as substrates for the KATI assay and 1 mM α-ketogluturate, 40μM pyridoxal 5'-phosphate (PLP) and 2 mM L-kynurenine as substrates for the KATII assay. Assays were incubated at 37 °C for 120 and 40 minutes respectively, and terminated with the addition of an equal volume of 350 mM ZnOAc, 50 mM NaOAc pH 5.4. Fluorescence intensity at 398 nM was measured following excitation at 344 nM.

Cell line authentication and mycoplasma testing

The authenticity of the HEK293 cells (Flp-In™-293 cells, Invitrogen) used to overexpress *huKMO* was confirmed as 100% concordant with HEK293 by STR-profiling (ISO15189 DANAK/ILAC accredited Identicell service, Aarhus University Hospital, Denmark). Transfected HEK293-*huKMO* cells were tested for mycoplasma periodically. For the batch of cells used in this assay the date of mycoplasma testing was 04/08/11; no mycoplasma contamination was detected. Cells used only as hosts for protein expression (Sf9 and *E. coli* strain

BL21(DE3)pLysS) were not formally authenticated after delivery from the supplier.

Crystallography

Crystallisation of P. fluorescens KMO and preparation of the inhibitor complex

Crystals of apo KMO were grown by hanging drop vapor diffusion at 4 °C using 1 µL protein at 12 mg/ml (in 20 mM HEPES pH 7.0, 20 mM Na acetate, 1 mM DTT) mixed with 1 µL crystallization reagent (0.1 M HEPES pH 7.0, 10% glycerol, 10% 2-propanol, 6.5% PEG 4000, 10 mM KCl) suspended over a 1 ml reservoir of the crystallization reagent. The newly set drops were streak seeded using a previously grown crystal crushed up into a few µL of reservoir solution. A crystal harvesting solution was prepared consisting of 1 part ethylene glycol to 4 parts crystallization reagent (0.1 M HEPES pH 7.0, 8% glycerol, 10% 2-propanol, 10% PEG 4000, 20 mM Na tartrate) to which GSK180 was added from a 50 mM stock solution in DMSO to give an overall concentration of 2.5 mM inhibitor and 5% DMSO. The harvesting solution was gradually added to the crystal drop to excess. After a few minutes, crystals were flash frozen in liquid nitrogen ready for data collection.

X-ray data collection and crystal structure determination

X-ray diffraction data (900 images, 0.2° oscillation range) were collected at 100 K using a Pilatus 6M detector at the European Synchrotron Radiation Facility (ESRF) beam line ID23-1. The data were processed and scaled using autoPROC[50], utilizing XDS[51], AIMLESS[52] and the CCP4 suite of programs[53]. The crystal space group is $P2_12_12$ with unit cell dimensions a = 186.9 Å, b = 105.3 Å, c = 133.6 Å, $\alpha = \beta = \gamma = 90°$. Data collection statistics are given in **Supplementary Table 5.** The structure was determined using the coordinates of an isomorphous unliganded *P. fluorescens* KMO model with preliminary refinement using autoBUSTER (BUSTER version 2.11.5. Global Phasing Ltd., Cambridge, U.K.). The ligand was clearly visible in the resulting Fo-Fc electron density map. Subsequent model building was carried out using Coot[54] and structure refinement was completed with autoBUSTER (R = 0.157, R_{free} = 0.196). The final model has been deposited in the Protein Data Bank under the accession code 5fn0.

Statistical analyses

We prospectively determined group sizes based on preliminary data, by using a pre-specified effect size of 2 points on the log scale for serum IL-6 as observed in historical experiments, estimating power $1-\beta=0.80$ and significance $z_{\alpha}=0.05$. Group sizes were increased to account for potential technical failures. Animals were allocated to experimental groups arbitrarily without formal randomization. There were no exclusion criteria. Investigators were not formally blinded to group allocation during the experiment or when assessing the outcome. We used the Kolmogorov-Smirnov test to compare data to the normal distribution. We analyzed normally distributed data using parametric two group (t-test) or multiple group analyses (one-way ANOVA with post-hoc Student-Newman-Keuls test) using SPSS v17.0.

Methods-only references

41. iKOMP. International_Knockout_Mouse_Project Number CSD40845. http://www.mousephenotype.org/martsearch_ikmc_project/martsearch/ikmc_project/40845. Accessed 06 April 2014.

42. Laukkarinen, J.M., Van Acker, G.J., Weiss, E.R., Steer, M.L. & Perides, G. A mouse model of acute biliary pancreatitis induced by retrograde pancreatic duct infusion of Na-taurocholate. *Gut* 56, 1590-1598 (2007).

43. Mole, D.J., McFerran, N.V. & Diamond, T. Differential preservation of lipopolysaccharide-induced chemokine/cytokine expression during experimental pancreatitis-associated organ failure in rats shows a regulatory expressed phenotype. *Pancreatology* 8, 478-487 (2008).

44. Schmidt, J.*, et al.* A better model of acute pancreatitis for evaluating therapy. *Annals of surgery* 215, 44-56 (1992).

45. Mole, D.J., Taylor, M.A., McFerran, N.V. & Diamond, T. The isolated perfused liver response to a 'second hit' of portal endotoxin during severe acute pancreatitis. *Pancreatology* 5, 475-485 (2005).

46. Van Laethem, J.L.*, et al.* Interleukin 10 prevents necrosis in murine experimental acute pancreatitis. *Gastroenterology* 108, 1917-1922 (1995).

47. Dragun, D.*, et al.* FTY720-induced lymphocyte homing modulates post-transplant preservation/reperfusion injury. *Kidney Int* 65, 1076-1083 (2004).

48. Studier, F.W. Protein production by auto-induction in high density shaking cultures. *Protein Expr Purif* 41, 207-234 (2005).

49. Wong, J., Ray, W.J. & Kornilova, A.Y. Development of a microplate fluorescence assay for kynurenine aminotransferase. *Anal Biochem* 409, 183-188 (2011).

50. Vonrhein, C.*, et al.* Data processing and analysis with the autoPROC toolbox. *Acta Crystallogr D Biol Crystallogr* 67, 293-302 (2011).

51. Kabsch, W. XDS. *Acta Crystallogr D Biol Crystallogr* 66, 125-132 (2010).

52. Evans, P.R. & Murshudov, G.N. How good are my data and what is the resolution? *Acta Crystallogr D Biol Crystallogr* 69, 1204-1214 (2013).

53. Winn, M.D.*, et al.* Overview of the CCP4 suite and current developments.*Acta Crystallogr D Biol Crystallogr* 67, 235-242 (2011).

54. Emsley, P., Lohkamp, B., Scott, W.G. & Cowtan, K. Features and development of Coot. *Acta Crystallogr D Biol Crystallogr* 66, 486-501 (2010).

Competing financial interest statement

The University of Edinburgh is engaged in a Discovery Partnership with Academia collaboration with GlaxoSmithKline. The University of Edinburgh receives milestone and royalty payments according to the phase of the project governed by the University of Edinburgh revenue sharing policy.

Figure 1.

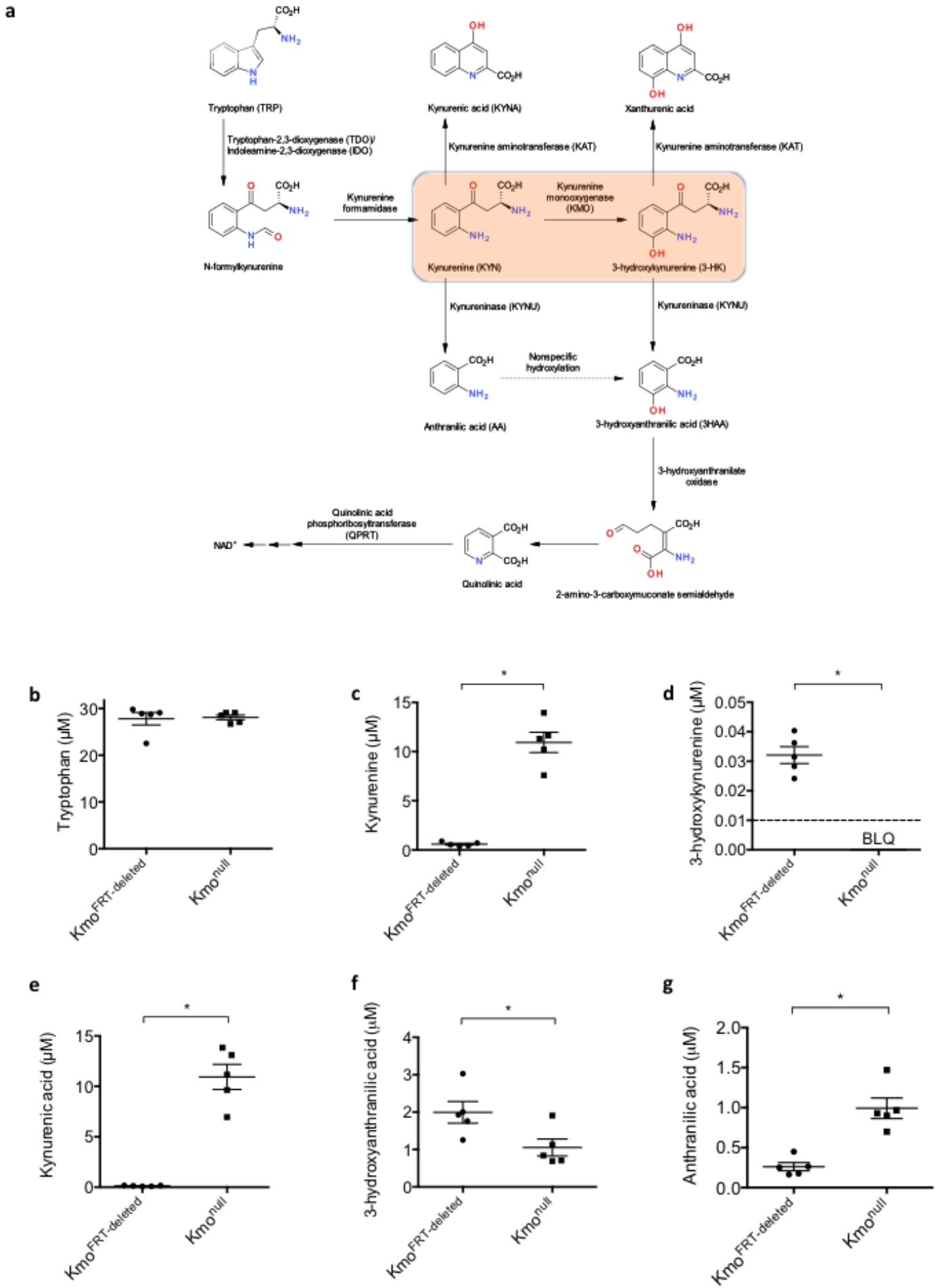
a
Tryptophan (TRP)
Kynurenic acid (KYNA)
Xanthurenic acid
Tryptophan-2,3-dioxygenase (TDO)/
Indoleamine-2,3-dioxygenase (IDO)
Kynurenine aminotransferase (KAT)
Kynurenine aminotransferase (KAT)
Kynurenine formamidase
Kynurenine monooxygenase (KMO)
N-formylkynurenine
Kynurenine (KYN)
3-hydroxykynurenine (3-HK)
Kynureninase (KYNU)
Kynureninase (KYNU)
Nonspecific hydroxylation
Anthranilic acid (AA)
3-hydroxyanthranilic acid (3HAA)
3-hydroxyanthranilate oxidase
Quinolinic acid phosphoribosyltransferase (QPRT)
NAD+
Quinolinic acid
2-amino-3-carboxymuconate semialdehyde
b
Tryptophan (μM)
c
Kynurenine (μM)
d
3-hydroxykynurenine (μM)
BLQ
e
Kynurenic acid (μM)
f
3-hydroxyanthranilic acid (μM)
g
Anthranilic acid (μM)
Kmo FRT-deleted
Kmo null

Figure 2

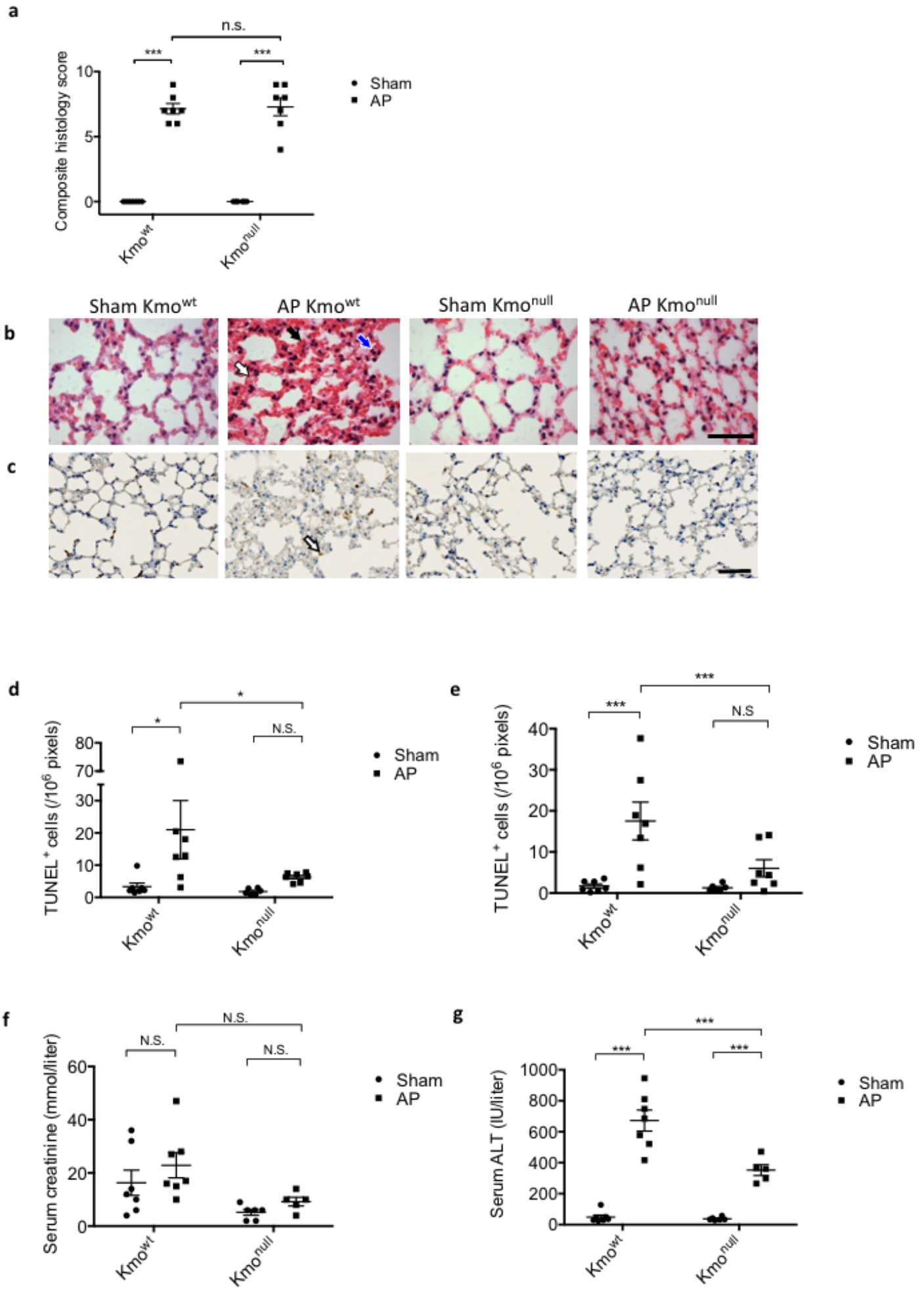
a
n.s.
***
***
Composite histology score
10
5
0
Sham
AP
Kmo^wt
Kmo^null
b
Sham Kmo^wt
AP Kmo^wt
Sham Kmo^null
AP Kmo^null
c
d
*
*
N.S.
TUNEL+ cells (/10^6 pixels)
80
70
30
20
10
0
Sham
AP
Kmo^wt
Kmo^null
e
***
***
N.S
TUNEL+ cells (/10^6 pixels)
40
30
20
10
0
Sham
AP
Kmo^wt
Kmo^null
f
N.S.
N.S.
N.S.
Serum creatinine (mmol/liter)
60
40
20
0
Sham
AP
Kmo^wt
Kmo^null
g
***
***
***
Serum ALT (IU/liter)
1000
800
600
400
200
0
Sham
AP
Kmo^wt
Kmo^null

Figure 3

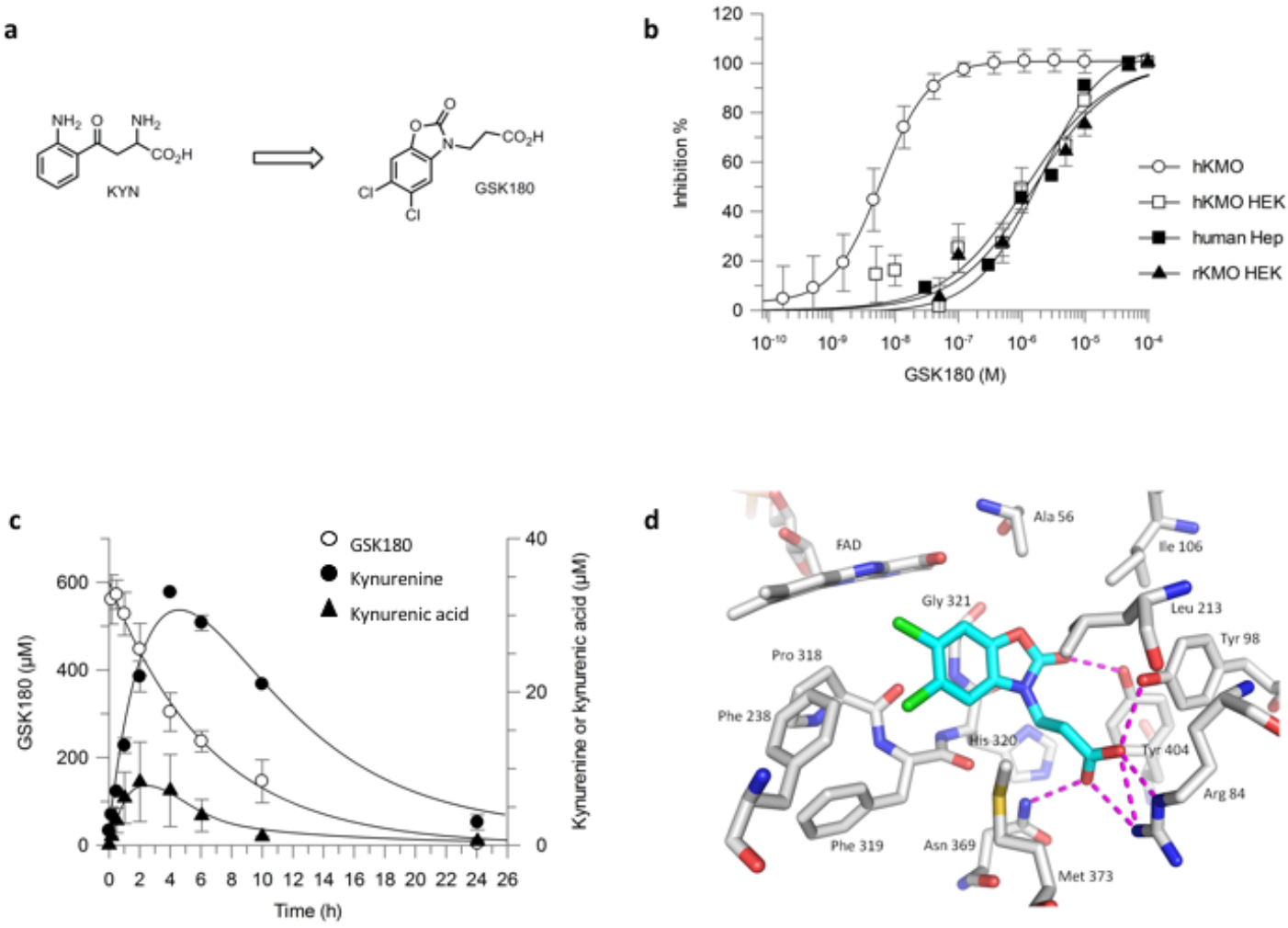
a
KYN
GSK180
b
Inhibition %
GSK180 (M)
hKMO
hKMO HEK
human Hep
rKMO HEK
c
GSK180 (µM)
Kynurenine or kynurenic acid (µM)
Time (h)
GSK180
Kynurenine
Kynurenic acid
d
FAD
Ala 56
Ile 106
Gly 321
Leu 213
Tyr 98
Pro 318
Phe 238
His 320
Tyr 404
Arg 84
Phe 319
Asn 369
Met 373

Figure 4

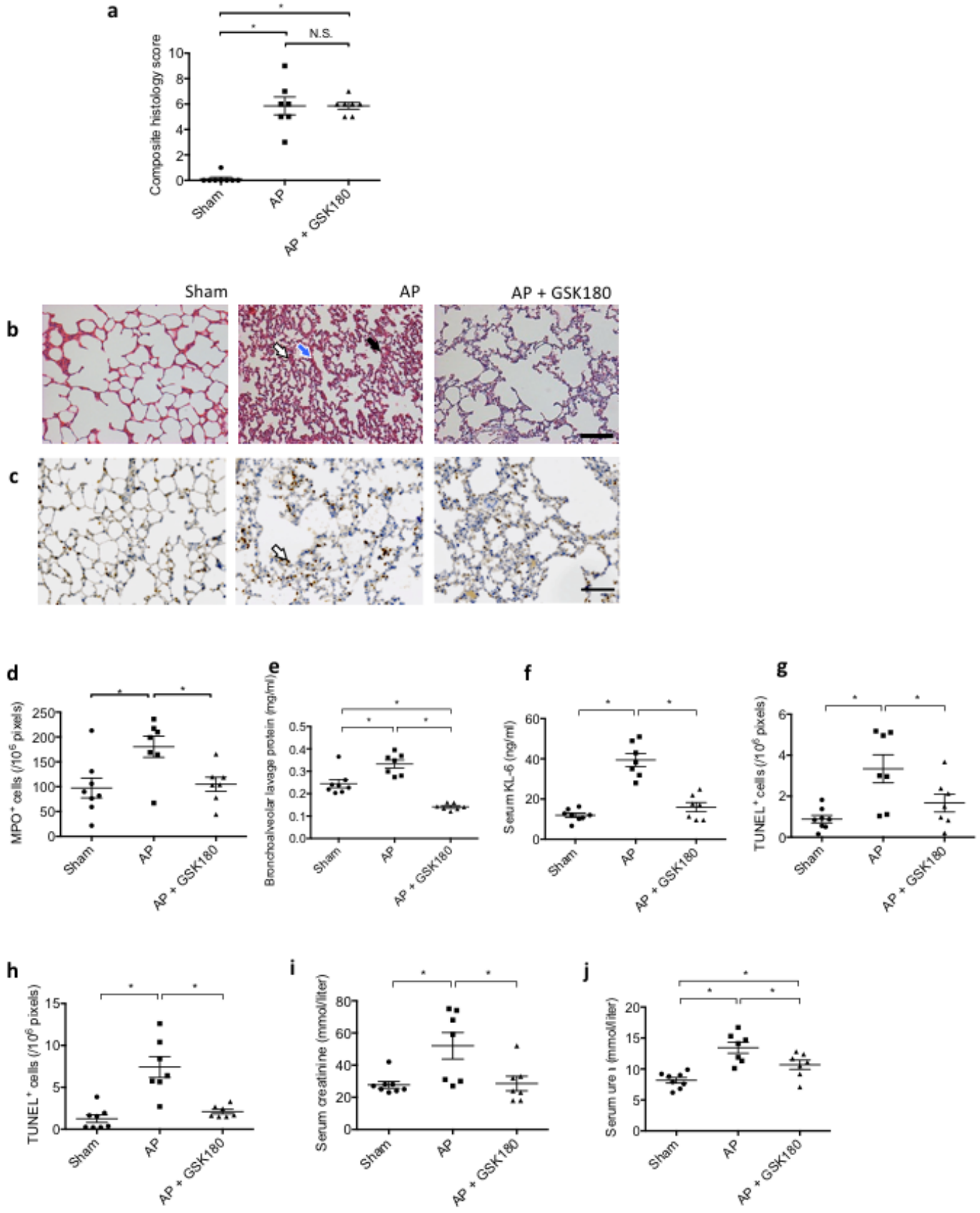
a
Composite histology score
N.S.
Sham
AP
AP + GSK180
b
Sham
AP
AP + GSK180
c
d
MPO+ cells (/10^6 pixels)
e
Bronchoalveolar lavage protein (mg/ml)
f
Serum KL-6 (ng/ml)
g
TUNEL+ cells (/10^6 pixels)
h
TUNEL+ cells (/10^6 pixels)
i
Serum creatinine (mmol/liter)
j
Serum urea (mmol/liter)